

Real-time machine learning-driven digital twin framework of a floating solar system in waves

Danlei Yang^{a,*}, Chenhao Mi^a, Xiangcheng Lyu^a, Ying Xie^b, Zhenhua Luo^a, Luofeng Huang^a

^a Faculty of Engineering and Applied Sciences, Cranfield University, Cranfield, UK

^b Faculty of Business and Management, Cranfield University, Cranfield MK430AL, UK

ARTICLE INFO

Keywords:

Floating photovoltaic
Digital twin framework
Real-time
Machine learning
Unity Real-Time Development Platform

ABSTRACT

Floating photovoltaic (FPV) systems offer a promising pathway for sustainable energy generation by avoiding land occupation, and utilising water cooling to improve energy efficiency. However, their deployment in dynamic aquatic environments introduces significant challenges, including irradiance fluctuations, hydrodynamic loads, and structural fatigue, which complicate reliable performance prediction. These highlight the need for advanced tools that can enable offshore structural monitoring, maintenance decision-making, and power management in a dynamic environment. To address these challenges, this study introduces a real-time digital twin framework for FPV systems, integrating laboratory experimentation, machine learning, and real-time visualisation. A bespoke facility combining a solar simulator, FPV prototype, and wave tank enabled 155 controlled tests under diverse irradiance and wave conditions. The resulting dataset was used to train a Random Forest model, which achieved an overall coefficient of determination of 0.990 and accurately predicted the dynamic responses of heave, surge, and pitch, with minimal discrepancies. The results were visualised through a real-time Unity-based user interface, enabling intuitive interaction and monitoring of the FPV system's behaviour. These findings demonstrate the potential of AI-enabled digital twins to enhance operational resilience, reduce maintenance costs, and pave the way for intelligent, adaptive control of large-scale offshore FPV deployments.

1. Introduction

The growing global demand for sustainable energy has accelerated the exploration of innovative technologies. Among them, floating photovoltaic (FPV) systems have emerged as a promising solution. Compared with conventional land-based photovoltaics, FPV systems exploit water surfaces, thereby reducing competition for land resources [1,2]. In addition, the thermal buffering effect of water enhances the cooling of photovoltaic modules, improving efficiency [3,4], whilst also enabling integration with existing hydrological infrastructure [5]. Several countries have already begun to deploy FPV installations at varying scales, according to Wood Mackenzie's Floating Solar Landscape 2024 report, the global installed FPV capacity is projected to reach 77 GW by 2033 [6]. And companies also have tested prototypes in near-shore environments [7,8], underscoring the sector's significant potential.

Despite these advantages, FPV deployment presents substantial challenges due to the dynamic nature of aquatic environments. Wave-induced motions can cause fluctuations in solar irradiance and

accelerate fatigue in structural connections and mooring systems [9,10]. To address these issues, research has primarily followed two approaches: experimental studies and numerical simulations. Experimental investigations have examined the dynamic response of FPV platforms under various wave conditions [8,11,12] and structural configurations [13–16], while numerical models have been employed to analyse wave–structure interactions through fluid–structure coupling techniques [17–19]. However, experimental studies are constrained by scale and controllability, whereas numerical simulations struggle to capture the complex interplay between geometry, environmental conditions and operational states. Furthermore, both approaches function predominantly as offline tools, lacking real-time adaptability, which limits their practical value for long-term offshore operation [20–22].

Digital twin technology has recently gained prominence as a novel engineering paradigm to overcome these limitations. A digital twin is a virtual counterpart of a physical system that remains dynamically synchronised via sensors and modelling techniques, enabling real-time prediction, monitoring and optimisation [23]. Applications already extend across multiple sectors: NASA employs digital twins for

* Corresponding author.

E-mail address: danlei.yang@cranfield.ac.uk (D. Yang).

<https://doi.org/10.1016/j.enconman.2026.121373>

Received 17 November 2025; Received in revised form 21 February 2026; Accepted 15 March 2026

Available online 20 March 2026

0196-8904/© 2026 The Author(s). Published by Elsevier Ltd. This is an open access article under the CC BY license (<http://creativecommons.org/licenses/by/4.0/>).

spacecraft monitoring, whilst companies such as General Electric (GE) and Chevron utilise them to enhance wind turbine operations [24]. Nonetheless, most conventional digital twins remain grounded in physics-based numerical simulations, which can be restrictive in highly dynamic or data-intensive environments. In the context of FPV, a digital twin has the potential not only to support accurate modelling but also to enable predictive maintenance, intelligent scheduling and real-time risk management. Such capabilities enhance system reliability and reduce the Levelised Cost of Energy (LCOE), thereby improving the competitiveness of offshore renewables [25–27].

Artificial intelligence (AI) offers a transformative extension to the digital twin concept. Unlike traditional physics-based models, AI can directly learn nonlinear system behaviours from data without requiring complete mathematical formulations [28]. In energy systems, AI techniques have already been widely applied to improve efficiency and optimise utilisation [28]. Several studies have explored the use of AI model for forecasting FPV performance [29–31], yet these efforts largely remain confined to offline predictions and rarely integrate with digital twin frameworks.

To bridge this gap, the present study proposes an AI-enabled digital twin framework for FPV systems. Fig. 1 illustrates the development of a real-time digital twin framework for a FPV prototype. On the left, the physical twin consists of an experimental FPV platform equipped with a motion sensor to capture dynamic responses, while a controllable light source simulates varying solar incidence angles. In the middle, sensor data are transmitted via communication channels to a digital twin environment, where a Unity-based 3D model visualises the live behaviour of the system, supported by a machine learning-driven Python framework for prediction and analysis. On the right, the system demonstrates both real-time synchronisation and future prediction: measured heave motion and power output are compared against machine learning forecasts, highlighting the framework’s capability to provide predictive insights beyond live monitoring. This integrated setup showcases the potential of digital twins for enhancing real-time analysis, visualisation, and forecasting in floating photovoltaic research. In this research, an experimental facility was developed, integrating a solar simulator, a floating PV unit and a wave tank, through which 155 controlled tests were conducted under diverse irradiance and wave conditions. Based on the resulting time-series dataset, a real-time digital twin framework was developed.

This integrated approach validates a novel FPV digital twin architecture that combines experimental measurement with data-driven modelling, highlights the potential of Random Forest techniques to deliver efficient and accurate prediction, and showcases the broader role

of digital twins in enhancing operational resilience, enabling real-time visualisation and reducing maintenance costs, ultimately advancing the development of intelligent and autonomous floating solar systems.

The remainder of this paper is structured as follows. Section 2 outlines the methodology, including visualisation strategies, machine learning techniques, and the development of a full-chain real-time digital twin framework. Section 3 focuses on the training of a Random Forest-based performance prediction model. Section 4 demonstrates the implementation of the real-time digital twin for the floating photovoltaic prototype. Section 5 provides a discussion on the future development of digital twin technologies in this context. Section 6 concludes the paper and highlights potential directions for further research.

2. Methodology

The methodology of this study integrates visualisation techniques, machine learning approaches, and a full-chain digital twin framework to enable real-time monitoring and prediction of FPV performance. First, visualisation methods are employed to represent both the physical prototype and its dynamic behaviour, including physical rendering in Unity and data-driven visualisation. Second, machine learning models, such as Random Forest, are applied to extract patterns from experimental datasets and historical records, thereby supporting predictive analytics. Finally, a comprehensive real-time digital twin framework is established, encompassing architecture design, sensor integration, coordinate system calibration, signal processing, sensor fusion, predictive modelling, visualisation optimisation, communication channels, and engineering robustness. Together, these methodological components provide a systematic foundation for building a reliable and predictive digital twin of the FPV prototype.

2.1. Visualisation methods

To effectively establish the link between the physical prototype and the digital twin, this study adopts two complementary visualisation strategies. The first focuses on physical rendering in Unity, where the structural features and dynamic responses of the FPV prototype are reproduced in a three-dimensional environment. The second highlights data visualisation, where real-time measurements and predictive outputs are presented through dynamic charts to facilitate interpretation and evaluation.

2.1.1. Physical visualisation in Unity

The physical visualisation of the FPV prototype was implemented in

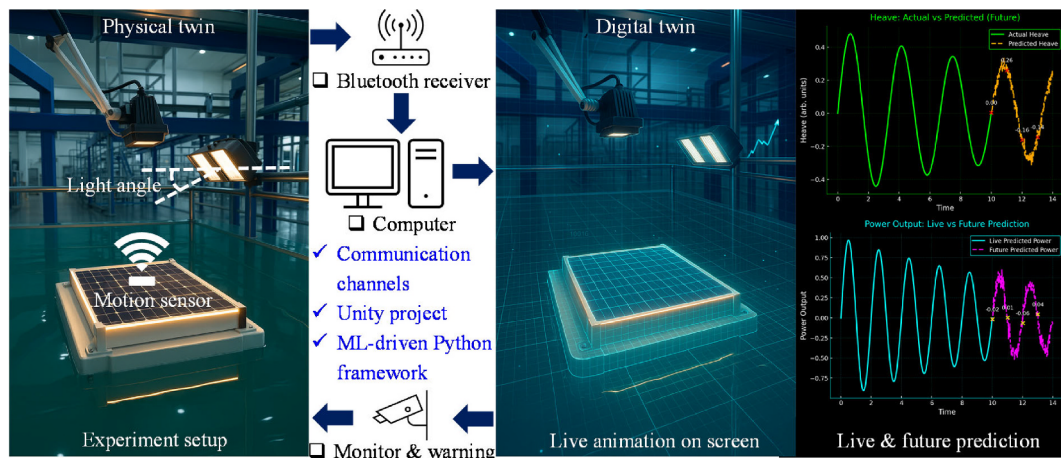


Fig. 1. Framework of a real-time digital twin for a floating photovoltaic prototype: (left) physical twin experimental setup with motion sensing and controlled light source; (middle) digital twin implementation with Unity visualisation and machine learning-based prediction; (right) real-time and future prediction of heave motion and power output.

a Unity three-dimensional environment. The modelling process incorporated the essential components of the system, including the solar model, the water surface, the photovoltaic panel, and the catamaran floater. Once constructed, the virtual scene allowed for the integration of environmental elements such as solar irradiation and water dynamics, providing a realistic representation of operating conditions. Fig. 2 shows the Unity-based physical visualisation of the FPV prototype.

2.1.2. Data visualization

The data visualisation module is designed to present the real-time dynamic responses of the FPV prototype together with system-level performance indicators. As shown in the Fig. 3, the platform monitors the primary motions of the system, including heave, surge, and pitch, which are plotted as time series to capture instantaneous variations. In addition, key operational variables such as power output, mooring forces, and photovoltaic panel temperature are displayed simultaneously.

2.2. Machine learning method with experiment data mining

The machine learning (ML) approach in this study is designed to predict the performance of the FPV prototype based on key operational parameters (also named as features in ML models), including light angles, wave frequency, wave amplitude, solar irradiance, heave, surge, pitch of the FPV. Historical experimental datasets are first pre-processed before being employed to train the models, ensuring that the underlying relationships between motion features and system responses are effectively captured. After achieving satisfactory ML performance through training, the model can be deployed in real time. Sensor-based motion features, such as heave, surge, and pitch, together with constant features such as light angle, wave frequency, wave amplitude, and solar irradiance, are fed into the model, which then predicts target variables, including power output, mooring forces, and panel temperature. Accordingly, Section 2.2.1 introduces the Random Forest method used to map motion features to target variables, while Section 2.2.2 describes the processing of historical data that underpins the model training.

2.2.1. Random Forest

Random Forest (RF) is chosen as the primary ML model because it provides a good balance of nonlinearity, robustness and interpretability for the FPV dataset. Compared with linear or polynomial regression, RF can capture stronger nonlinearities and interactions between motion and environmental features. Compared with SVM and XGBoost, RF is less sensitive to hyperparameter tuning and works reliably on our medium-sized, noisy experimental data without requiring extensive optimisation. Compared with neural networks, RF achieves satisfactory accuracy with a much simpler training procedure and offers clearer feature-importance measures, which is beneficial for a physics-informed digital twin. RF works by building an ensemble of decision trees, each trained on a random subset of the data and features, and combining their

outputs through averaging, as shown in Fig. 4. This mechanism reduces variance, limits overfitting, and captures nonlinear relationships between inputs and outputs. In this study, historical datasets are used to train a RF model to map motion parameters (heave, surge, and pitch) to performance indicators, such as power output, mooring forces, and panel temperature.

The RF algorithm operates as an ensemble of K regression trees. Given an input feature vector x , the forest aggregates the predictions of all trees to produce the final output y through averaging:

$$y = \frac{1}{K} \sum_{k=1}^K h_k(x) \quad (1)$$

where $h_k(x)$ represents the output of the k -th independent decision tree. The optimization of each tree's structure involves identifying the optimal split at each node by minimizing the Mean Squared Error (MSE) criterion:

$$MSE = \frac{1}{n} \sum_{i=1}^n (y_i - \bar{y})^2 \quad (2)$$

where n is the number of samples in the node, y_i are the observed values from the physical experiments, and \bar{y} is the mean value of those samples. The machine learning pipeline was implemented in Python 3.9 utilizing the Scikit-learn library [32].

The predictive framework utilizes a RF regressor, an ensemble learning method that constructs a multitude of decision trees during the training phase. In this study, the ensemble consists of 600 independent decision trees, a size determined by evaluating the stability of the prediction error across various configurations. Each tree is trained on a unique data subset generated via bootstrapping—a sampling technique with replacement that ensures each tree is exposed to a distinct distribution of the training data. This diversity within the ensemble enhances the model's overall robustness and reduces the risk of overfitting. At each node split within the trees, a random subset of 10 features is evaluated to identify the optimal partition, ensuring the model effectively captures the nonlinear interactions between wave parameters, solar irradiance, and FPV performance. To maintain maximum predictive fidelity, the maximum depth of the trees is set to 'None', allowing them to grow until the leaves reach maximum purity.

Furthermore, a sensitivity analysis was conducted to evaluate the impact of the tree depth configuration on the model's predictive performance. While a constrained depth (e.g., $\text{max_depth} = 10$) significantly reduces the complexity of the forest, it leads to a marked decrease in fidelity, with the average coefficient of determination (R^2) dropping from 0.9904 to 0.9191. Conversely, the performance for $\text{max_depth} = 100$ was found to be identical to the unconstrained configuration ($\text{max_depth} = \text{None}$), indicating that the ensemble naturally converges as the leaves reach their optimal purity before exceeding this depth. These results justify the use of an unconstrained depth setting, which ensures that the digital twin can accurately map the intricate physical

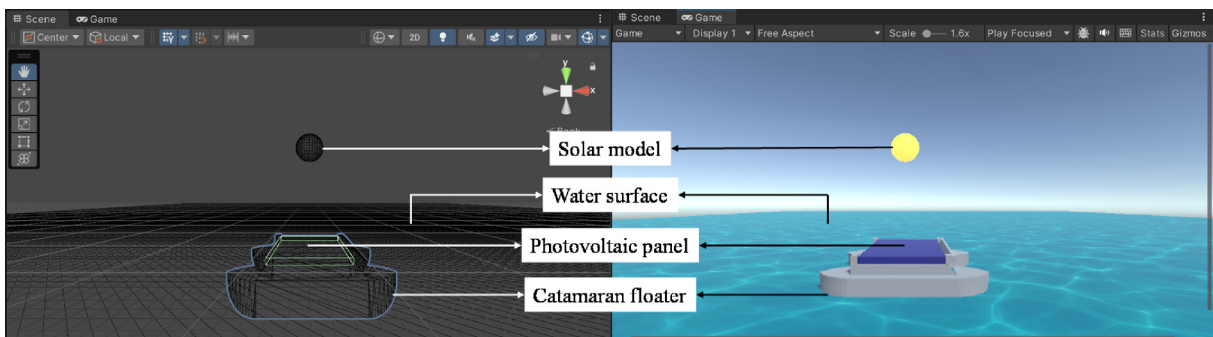


Fig. 2. Physical visualisation of the floating photovoltaic prototype in Unity, showing the solar model, water surface, photovoltaic panel, and catamaran floater.

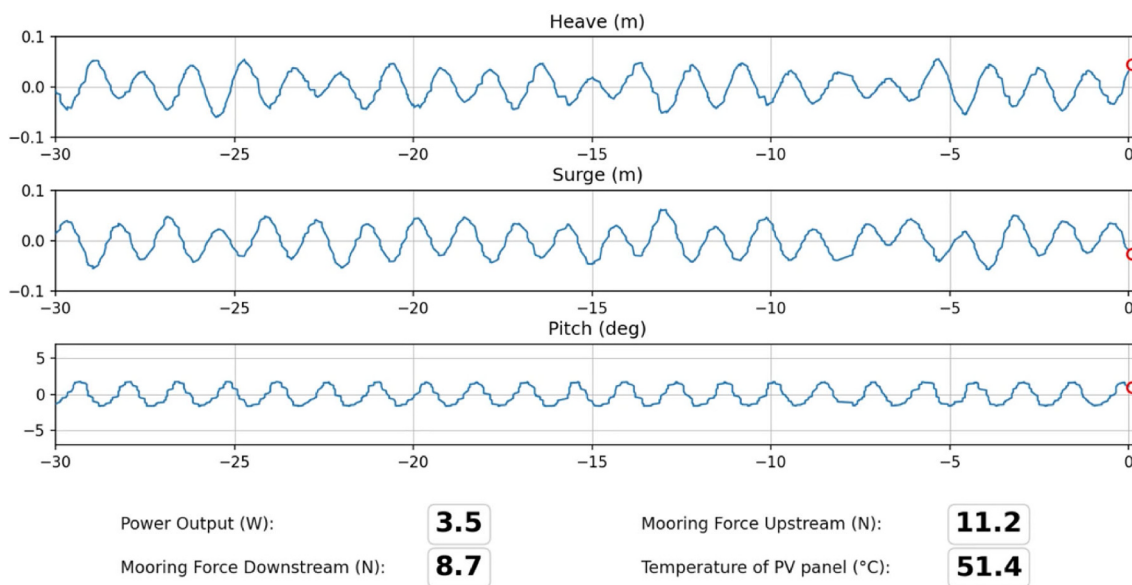


Fig. 3. Data visualisation interface displaying real-time motion responses (heave, surge, and pitch) alongside predicted variables including power output, mooring forces, and photovoltaic panel temperature.

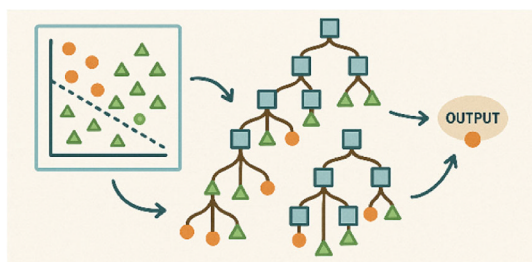


Fig. 4. Schematic illustration of the Random Forest model, showing the ensemble of decision trees and the aggregated output.

behaviours of the FPV system without introducing artificial bias through excessive pruning.

Note that, the selection of RF was justified through a comparative benchmark against other popular machine learning architectures, including HistGradientBoosting (HistGB), Long Short-Term Memory (LSTM) networks, Convolutional Neural Networks (CNN). Although HistGB offered a shorter training time (approx. 15 min), its average R^2 of 0.9639 was lower than that of the RF model (0.9904, 30 min training). Furthermore, complex deep learning models like LSTM, while capable of handling temporal sequences, required significantly higher computational overhead (approx. 2 h) without providing additional gains in predictive fidelity. Given the requirement for both high precision and real-time responsiveness in a digital twin interface, RF was determined to be the most suitable algorithm for mapping the FPV system's performance.

2.2.2. Historical data processing

To enable the training of machine-learning models, a series of laboratory experiments were conducted on a FPV prototype in a controlled wave tank. The experimental arrangement is shown in Fig. 5 and the parameters are shown in Table 1, from which the historical dataset for this study was obtained.

The water tank measures 30 m × 1.5 m × 1.5 m (fresh water), generates regular waves with 0.1–1.1 Hz frequency and up to 28 cm height via a three-paddle wavemaker (Edinburgh Designs), and employs a full-width parabolic beach to suppress reflections. The FPV unit was moored at four corners; mooring lines consisted of a fishing line + spring

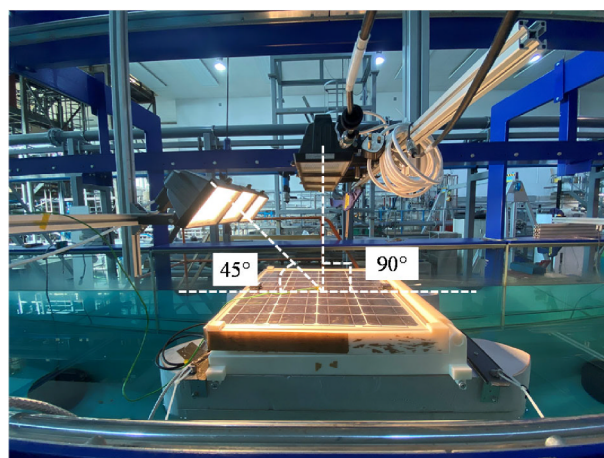


Fig. 5. Experimental setup of the FPV prototype in the wave tank, showing the catamaran floater, photovoltaic panel, solar simulator lamps, and sensor arrangement.

(initial spring length 18.3 cm, stiffness 454.5 N m⁻¹, total line length 220 cm), with the longitudinal anchor distance set to 150 cm; preload forces were measured and equalised. A solar simulator made from three Eterna CTH500SL 500 W halogen floodlights was mounted 400 mm above the panel and calibrated so the PV produced 30 W under still water. The PV module (TDG T050M365, 50 W max) was installed on a newly designed catamaran floater using XPS (density 38.44 kg m⁻³, compressive strength 64.6 psi).

Multi-domain measurements were recorded at 10 Hz unless noted: upstream/downstream mooring forces (Vernier Go Direct Force & Acceleration, with RS PRO steel extension springs; Vernier Graphical Analysis); motions—heave, surge, pitch—using Witmotion accelerometer-inclinometers (two units on the PV, upstream and downstream); temperatures (ambient, water, PV centre) via thermocouples (PicoLog); surface elevation using two PEPPERL + FUCHS 60947-5-2 ultrasonic sensors (LabVIEW); power output with EL 9000 B Electronic DC Load (EA Power Control; triangular protocol: $U(A) = 22.83 \text{ V}$, $t_1=0.05 \text{ ms}$, $t_2=0.05 \text{ ms}$, $I_{\text{limit}} = 2.94 \text{ A}$, $P_{\text{limit}} = 50 \text{ W}$); and irradiance using an RS PRO ISM410 solar power meter (one-off readings

Table 1
Parameters for the experimental arrangement.

Category	Parameter	Value/Setting	Notes
Water tank & waves	Tank dimensions	30 m × 1.5 m × 1.5 m	Fresh water
	Wave type	Regular waves	
	Wave frequency range	0.1–1.1 Hz	Generated by wavemaker
	Wave height (max)	up to 0.28 m (28 cm)	
Mooring system	Wavemaker	Three-paddle wavemaker (Edinburgh Designs)	
	Wave absorption	Full-width parabolic beach	To suppress reflections
	Mooring configuration	Four-corner mooring	FPV moored at four corners
	Mooring line composition	Fishing line + spring	
Solar simulator	Spring initial length	18.3 cm	
	Spring stiffness	454.5 N m ⁻¹	RS PRO steel extension springs
	Total line length	220 cm	Per mooring line
	Longitudinal anchor distance	150 cm	Along tank length
	Preload forces	Measured and equalised	
	Light source	Three Eterna CTH500SL halogen floodlights	500 W each
PV module & floater	Mounting height	400 mm above PV panel	
	Calibration condition	PV output 30 W under still water	Used as reference condition
	PV module model	TDG T050M365	Nominal 50 W max
	PV rated power	50 W (max)	
Sampling & logging	Floater type	Catamaran-type floater	Newly designed
	Floater material	XPS (extruded polystyrene)	
	XPS density	38.44 kg m ⁻³	
	XPS compressive strength	64.6 psi	
Mooring forces	Sampling rate (general)	10 Hz	Unless otherwise noted
	Sensors	Vernier Go Direct Force & Acceleration	Upstream and downstream
	Springs	RS PRO steel extension springs	In series with force sensors
Motions (heave/surge/pitch)	Software	Vernier Graphical Analysis	Data acquisition
	Sensors	Witmotion accelerometer-inclinometers	Two units on PV
	Sensor locations	Upstream and downstream ends of PV panel	
Temperatures	Quantities measured	Ambient air, water, PV centre temperature	
	Instrument	Thermocouples with PicoLog	
Surface elevation	Sensors	Two PEPPERL + FUCHS 60947–5-2 ultrasonic sensors	Upstream/downstream surface elevation
	Acquisition	LabVIEW	
Power output	Load device	EL 9000 B Electronic DC Load	EA Power Control
	Protocol type	Triangular protocol	
	Protocol parameters	U(A) = 22.83 V; t ₁ = 0.05 ms; t ₂ = 0.05 ms;	

Table 1 (continued)

Category	Parameter	Value/Setting	Notes
Irradiance	Instrument	I _{limit} = 2.94 A; P _{limit} = 50 W RS PRO ISM410 solar power meter	
	Measurement method	One-off readings at three PV locations, averaged	Calibration/monitoring
Experimental matrix	Total number of cases	155 cases	
	Light incidence angles	90°, 75°, 60°, 45°, 30°	5 levels
	Wave amplitudes	0.025 m, 0.0375 m	2 levels
	Wavelength range	1.5–5.0 m in 0.25 m steps	15 levels
	Control group (quiescent water)	Same 5 light angles, amplitude = 0, wavelength = 0	No waves
	Purpose	Broad operating envelope for coupled hydro-mechanical–electro-thermal behaviour	For ML/digital-twin training

at three panel locations, averaged).

A total of 155 cases were executed. The experimental matrix combined five light incidence angles (90°, 75°, 60°, 45°, 30°) with two wave amplitudes (0.025 m, 0.0375 m) and fifteen wavelengths (1.5–5.0 m in 0.25 m steps). The control group repeated the five angles under quiescent water (amplitude = 0, wavelength = 0). This plan yielded a broad operating envelope for learning coupled hydro-mechanical–electro-thermal behaviours.

For each case, all sensors were powered and synchronised to UK local time; the wavemaker was initialised to the prescribed amplitude–frequency pair; once the wave field stabilised, data were recorded continuously for 2 min at 10 Hz under steady conditions. This produced aligned, high-resolution time series across mechanics, temperature, irradiance, and electrical output.

Raw streams were converted to.xlsx and assembled per case into a single file; timestamps were synchronised (UK local time). A clean 90-second valid segment was extracted and erroneous entries removed. Motion channels were further processed to derive heave and surge displacements from the recorded signals. Finally, all parameters were merged into a unified dataset formatted for direct ingestion by Random Forest in Section 2.2.1.

Further details of the experimental setup are provided in the Appendix 2.

2.3. Real-time digital twin framework

The overall architecture of the real-time digital twin is illustrated in Fig. 6. Motion data from the sensor are transmitted via a Bluetooth transceiver and first processed in Python Module 1, which handles socket communication and data decoding. Once decoded, the live motion signals are distributed across multiple processing branches. Python Module 2 manages data storage and provides live plots of the raw motion signals, ensuring both visual monitoring and experimental archiving. Python Module 3 applies pre-trained machine-learning models (see Section 2.2) to predict unmeasured performance indicators such as photovoltaic power output, mooring forces, and panel temperature, which are simultaneously visualised in real time. Python Module 4 further extends this capability by forecasting short-term future motions, allowing the live plots to include predicted trajectories alongside measured ones. In parallel, the live motion signals are transmitted through Python–Unity interface scripts to the Unity environment. Unity provides a three-dimensional visualisation of the FPV prototype, synchronised with the measured motions. This ensures a clear separation between physical synchronisation (Unity) and predictive

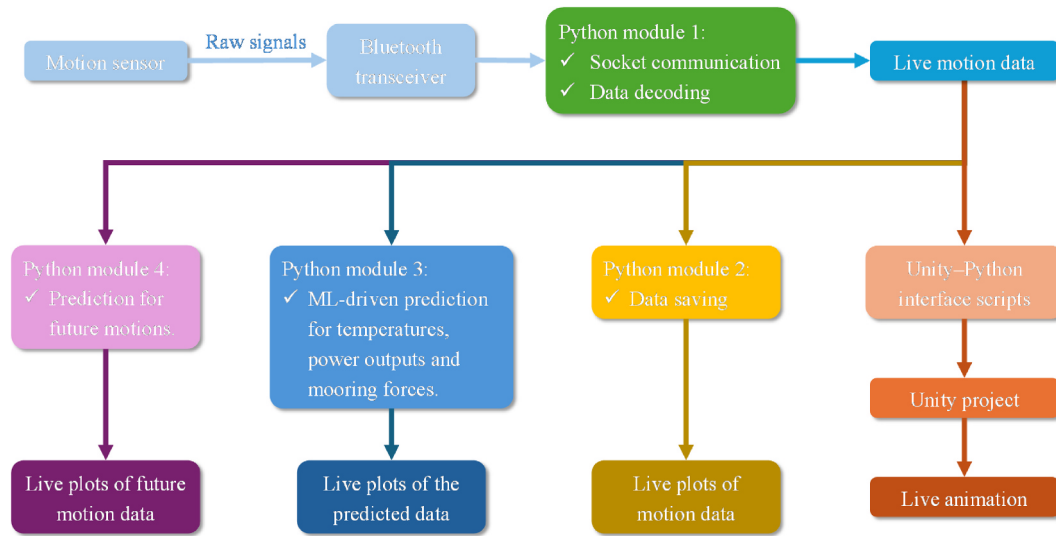


Fig. 6. Real-time digital twin framework for the FPV prototype.

intelligence (Python), while together delivering an integrated digital twin framework for real-time monitoring and analysis.

To present the framework systematically, the following subsections respectively describe: 2.3.1 the overall architecture and data flow; 2.3.2 the sensor suite and WT901 decoding; 2.3.3 coordinate frames and gravity compensation; 2.3.4 signal processing and drift suppression; 2.3.5 dual-sensor fusion; 2.3.6 prediction and the AI panel; 2.3.7 visualisation performance optimisation; 2.3.8 communication and logging; and 2.3.9 engineering robustness.

2.3.1. Architecture & data flow

The real-time digital twin system is organised as a two-IMU pipeline that ensures accurate motion acquisition, robust processing, and parallel execution of downstream tasks. Two WT901 sensors continuously transmit six-degree-of-freedom motion data via Bluetooth Low Energy (BLE). The signals are first decoded and processed through single-sensor motion analysis, including gravity compensation, filtering, and numerical integration. The outputs from both sensors are then averaged to suppress noise and mitigate drift, producing a stable and reliable motion reference.

The averaged motion stream is distributed to several modules in parallel. Through a TCP socket, the data are synchronised with the Unity environment, where they drive a real-time three-dimensional animation of the FPV prototype. In addition, the same data are rendered with Matplotlib for real-time visualisation and asynchronously logged into CSV files for permanent storage and offline analysis. Meanwhile, a background prediction panel calls pre-trained AI models, which use the live motion signals as inputs to predict performance indicators such as power output, mooring forces, and photovoltaic panel temperature.

To coordinate these concurrent processes, the framework employs asynchronous and multithreaded execution. An asyncio event loop manages scheduling, while independent threads are responsible for Unity listening, CSV writing, and AI inference. A producer-consumer queue is further introduced to regulate data throughput, preventing bottlenecks and ensuring smooth, low-latency performance across all subsystems.

2.3.2. Sensors & decoding (WT901)

The real-time digital twin relies on dual WT901 inertial measurement units (IMUs), which continuously provide six-degree-of-freedom motion data. The raw output is transmitted as binary frames via Bluetooth Low Energy (BLE). Each frame is identified by a fixed header sequence 0x55 0x61 and has a constant length of 20 bytes, which allows

reliable segmentation of the data stream and robust frame parsing.

After frame detection, the binary payload is decoded into physical quantities. These include linear accelerations (a_x , a_y , a_z), angular velocities (w_x , w_y , w_z), and Euler angles (roll, pitch, yaw). The sensor encodes these quantities in fixed-point format, which are subsequently converted into International System of Units (SI) for acceleration ($m \cdot s^{-2}$), angular velocity ($rad \cdot s^{-1}$), and degrees for orientation. This conversion ensures that the decoded signals can be consistently integrated with the data processing modules, enabling accurate motion analysis, gravity compensation, and integration steps in the pipeline.

2.3.3. Coordinate system & gravity compensation

To ensure consistent motion analysis, sensor outputs are transformed between the body-fixed and world coordinate systems. The Euler angles (roll, pitch, yaw) reported by the WT901 are first converted into a Direction Cosine Matrix (DCM) using the `euler_deg_to_dcm` routine. This transformation matrix enables bidirectional mapping between the body frame, where the raw accelerometer readings are defined, and the global world frame, in which physical motion is interpreted.

A key step in the pipeline is gravity compensation. Since accelerometer signals inherently include the effect of gravity, the estimated gravity vector is computed from the orientation and expressed in the body frame. This gravity component is subtracted from the raw accelerations, thereby isolating the linear acceleration caused by platform motion. The resulting signals are then transformed back into the world coordinate system, providing drift-minimised acceleration data suitable for integration and subsequent displacement estimation.

2.3.4. Signal processing & drift suppression

The processing of inertial signals is designed to reduce noise and mitigate integration drift, thereby enabling stable estimation of displacement. A combination of custom one-pole filters, thresholding, and zero-velocity-inspired resets are employed.

Firstly, one-pole filters are implemented to form a band-pass effect. For acceleration signals, a high-pass filter (HPF) suppresses constant bias and slow-varying offsets, while a subsequent low-pass filter (LPF) attenuates high-frequency noise. For velocity, which is obtained through numerical integration of acceleration, an additional HPF is applied to suppress slow drift. For displacement, a further HPF stage is introduced to limit accumulated errors and enhance long-term stability.

Secondly, a deadband operation is applied to the acceleration channel, where values below a defined threshold are set to zero. This suppresses micro-level noise and prevents its amplification through

integration.

Thirdly, a ZUPT-like mechanism (Zero-Velocity Update inspired) is incorporated. Static phases are detected by evaluating the norms of acceleration and angular velocity within a moving time window. Once a stationary condition is confirmed, velocity estimates and filter states are reset, effectively removing accumulated drift.

Finally, an adaptive time-step (dt) strategy is adopted. The first sample is processed using an assumed sampling rate (fs_{assumed}), while subsequent time-steps are derived from timestamp differences. Upper and lower bounds are enforced to avoid anomalies, ensuring robust numerical integration across varying runtime conditions.

2.3.5. Dual-sensor fusion

To improve the reliability of motion estimation, the framework integrates data from two WT901 inertial measurement units (IMUs) positioned at the upstream and downstream ends of the FPV prototype. After individual decoding and processing, the corresponding motion quantities, particularly heave, surge, and pitch, are fused using a simple arithmetic mean. This averaging strategy effectively reduces random noise and alleviates sensor-specific bias, producing a more stable estimate of the system's motion. By applying this lightweight fusion method, the digital twin achieves improved robustness without introducing the complexity of advanced filtering or sensor fusion algorithms, while still providing sufficiently accurate inputs for synchronisation, visualisation, and prediction tasks.

2.3.6. Prediction & AI panel

The prediction module extends the digital twin by augmenting live measurements with both short-term forecasts and machine-learning inference. A 0.1 s forecast dot is generated using linear extrapolation of the most recent two data points, providing a near-future trajectory marker that enhances situational awareness of dynamic responses.

In parallel, machine-learning inference is performed in a dedicated background thread. A pre-trained model pipeline, loaded via Joblib, supports Random Forest prediction. To avoid excessive computational load, inference is throttled by a `max_fps` parameter. The predicted results are safely transferred back to the main thread using `call_soon_threadsafe`, ensuring non-blocking updates to the user interface.

A lightweight AI panel is integrated into the visualisation environment, positioned at the bottom of the data visualisation interface, as shown in Fig. 3. It continuously displays the predicted values of performance indicators such as power output, mooring forces, and temperature, offering users an immediate overview of the system's physical state as estimated by the machine-learning models.

2.3.7. Communication & logging

A lightweight communication bridge is implemented to synchronise data between the Python processing pipeline and the Unity visualisation environment. A TCP socket server is established within Python, streaming motion data as JSON-formatted lines. This design allows Unity to act as a client, continuously receiving and rendering the decoded signals in real time. The use of structured JSON packets ensures both human readability and compatibility with downstream parsing.

In parallel, a dedicated asynchronous CSV logger is deployed to maintain a complete experimental record. Motion and prediction outputs are passed into a producer-consumer queue, which is served by a background thread. Data are periodically flushed to disk to balance performance and reliability, reducing I/O latency during real-time execution. Separate CSV files are maintained for different categories, including raw sensor outputs, processed results, and averaged values. This modular logging scheme supports both rapid debugging and systematic post-processing, while guaranteeing that no data are lost during concurrent visualisation and prediction tasks.

2.3.8. Engineering robustness

To ensure stable operation under practical runtime conditions,

several engineering measures were introduced to strengthen the robustness of the digital twin framework.

Firstly, Windows Asencio adaptation was applied to address compatibility issues between asynchronous event loops and Bluetooth libraries on Windows platforms. The Windows Selector Event Loop Policy was explicitly enforced, together with single-threaded apartment (STA) support for the Bleak/WinRT stack, ensuring reliable sensor communication across different environments.

Secondly, thread allocation was constrained by defining environment variables such as `OMP_NUM_THREADS` and `OPENBLAS_NUM_THREADS`. This limits the number of threads spawned by numerical backends (OMP/BLAS), preventing uncontrolled CPU contention and preserving real-time responsiveness of the main pipeline.

Finally, rate limiting and backpressure control were implemented for the AI inference queue. The queue length was fixed at one, and any outdated requests were cleared before new data were enqueued. This design prevents backlog accumulation, ensures that predictions remain synchronised with live data, and avoids memory growth over extended operation.

Together, these engineering refinements guarantee that the framework maintains consistency, responsiveness, and reliability in real-time applications.

3. Results and discussion

3.1. Random Forest-based performance prediction

The predictive capability of the RF model was assessed across all performance indicators, including power output, PV panel temperature, and upstream and downstream mooring forces. As summarised in Table 2, the model achieved coefficients of determination (R^2) exceeding 0.98 for all outputs, with an overall average of 0.990. The RF model achieved consistently high performance on both the training and test sets (average train $R^2 = 0.999$, test $R^2 = 0.990$), with only a small gap between them, indicating no obvious overfitting and good generalisation to unseen data. These consistently high values confirm the strong ability of the RF framework to capture both electrical-thermal responses and mechanical loads.

The parity plots in Fig. 7 further illustrate the model's accuracy. Power output and PV panel temperature predictions are tightly clustered along the 1:1 line, indicating excellent agreement with true values. A small degree of banding is visible in the power output, arising from discretised light-angle inputs, while the temperature predictions exhibit near-perfect alignment, apart from a few mid-range outliers. Mooring force predictions display greater variability. The upstream force is more challenging, with heteroscedasticity and larger deviations at high amplitudes, reflecting the non-linear nature of wave-structure interactions. Downstream force predictions are comparatively tighter, with only moderate scatter at the extremes.

Complementary evidence is provided by the time series comparisons in Fig. 8, which demonstrate the model's ability to reproduce dynamic variations over a 20-second window. For power output and PV panel temperature, the predicted signals almost completely overlap with the true series, showing negligible phase lag or amplitude error. Upstream mooring force predictions capture the oscillatory pattern but tend to

Table 2

Coefficient of determination (R^2) of Random Forest predictions for power output, PV panel temperature, and upstream and downstream mooring forces.

Target	Coefficient of determination (R^2)
Power output/W	0.994
Temperature of PV panel/ $^{\circ}\text{C}$	0.999
Mooring force upstream/N	0.986
Mooring down upstream/N	0.982
Average	0.990

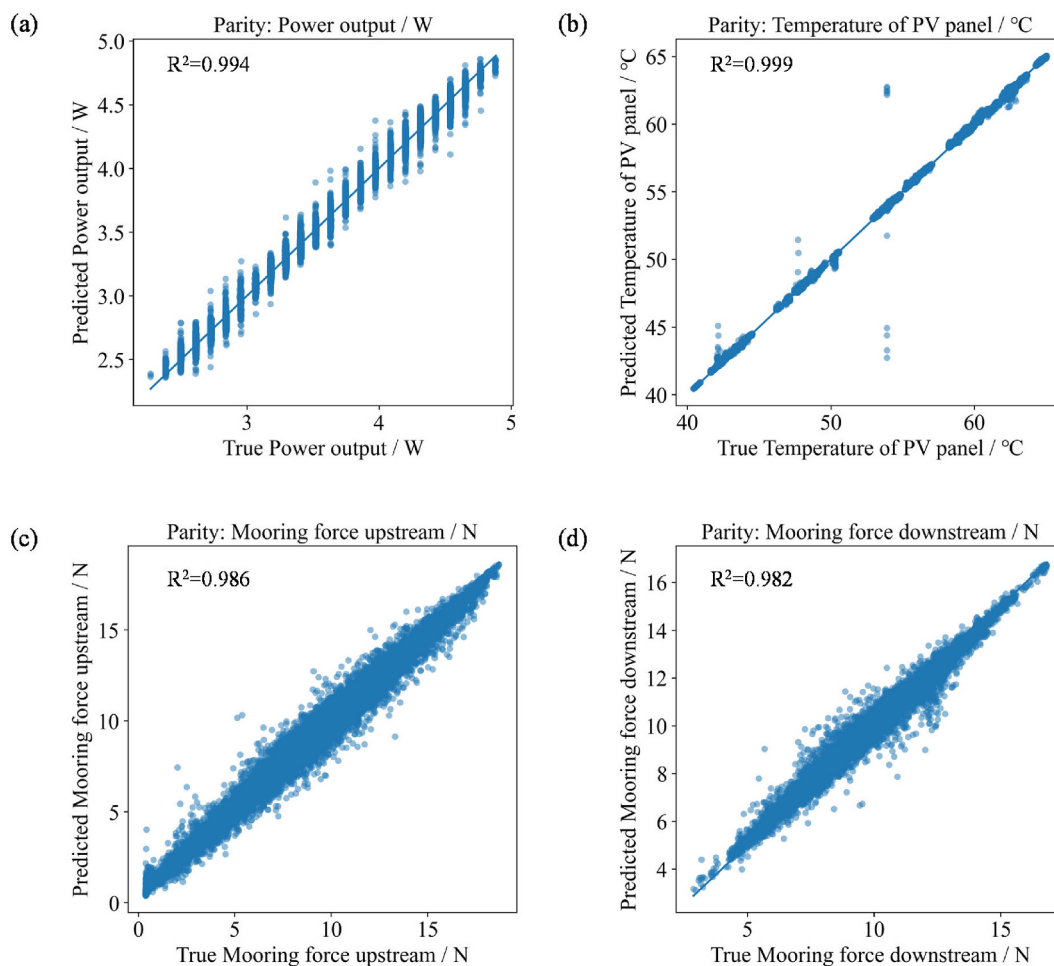


Fig. 7. Parity plots of Random Forest predictions versus true values for all performance targets: power output, PV panel temperature, and upstream and downstream mooring forces.

underestimate peak magnitudes. Downstream mooring force predictions remain more stable, closely tracking the true oscillations throughout the interval.

Overall, the RF model delivers highly accurate predictions for power and temperature, while providing acceptable fidelity for mooring forces. These results validate the RF model as a reliable surrogate for subsequent sensitivity analysis.

To further verify the generalization capability of the model and ensure the high R^2 was not a result of data leakage, a more rigorous validation was performed. Following the split ratio suggested by the independent validation protocols, the 155 physical experimental datasets were partitioned into 150 cases for training and 5 cases for independent testing (representing approximately 3.2% of the total samples). As summarized in Table 3, the model demonstrated exceptional stability, with the average R^2 slightly increasing from 0.990 under the original 80/20 split to 0.992 under the 150/5 split. This robust performance is attributed to the high-fidelity nature of the controlled wave tank measurements and the model's ability to capture the underlying deterministic physics.

3.2. Sensitivity of performance targets to input features

A global variance-based sensitivity analysis was carried out using Sobol' indices, with the results summarised in Fig. 9. Two indices are reported: the first-order index (S1), which quantifies the proportion of variance in the output explained by a given input in isolation, and the total-effect index (ST), which accounts for both its main effect and all

higher-order interactions. The difference between ST and S1 therefore provides a measure of the extent to which an input contributes through interactions with other factors.

For power output, as shown in Fig. 9(a), the dominant influences are light angle and solar irradiance, particularly the middle and right irradiance sensors. Their S1 and ST values are almost identical, suggesting that their effects are primarily additive with little contribution from interactions. While wave-induced oscillations of the PV panels (approximately $\pm 4^\circ$) alter the instantaneous incident solar radiation, their overall impact on power generation remains secondary under the tested conditions. This is primarily due to the high wave frequencies observed (0.54–1.02 Hz), which result in rapid oscillation cycles that have a limited effect on the cumulative power output trend. Sensitivity analysis, as shown in Fig. 9(a), confirms that the influence of motion-related variables is an order of magnitude lower than that of solar irradiance and incident angles. Consequently, while these factors are integrated into the system, they are considered secondary drivers in the predictive model. For PV panel temperature (in Fig. 9(b)), the sensitivity pattern closely mirrors that of power output. Again, light angle and irradiance dominate, with S1 and ST nearly coincident, indicating a purely additive role. This similarity in sensitivity explains the strong positive correlation typically observed between power and panel temperature.

For upstream mooring force (in Fig. 9(c)), the most influential input is heave motion, with S1 exceeding 0.5 and ST approaching 0.7. The moderate gap between ST and S1 highlights that heave not only contributes independently but also interacts with other variables. Surge and

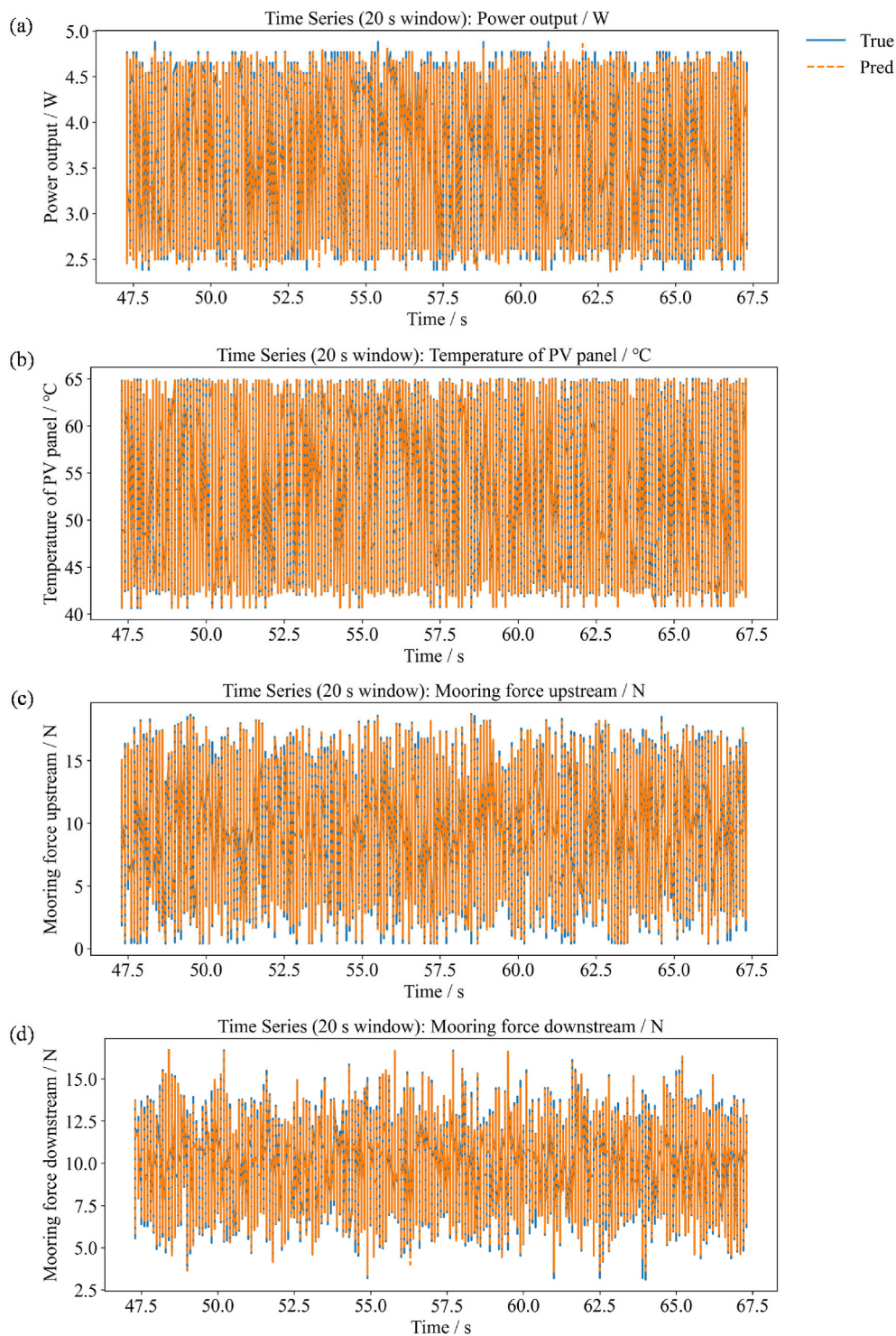


Fig. 8. Time series comparison of Random Forest predictions and true values within a 20-s window for power output, PV panel temperature, and upstream and downstream mooring forces.

wave amplitude provide secondary contributions: their S1 values are close to zero, yet their ST indices are elevated, showing that they influence upstream load mainly through interactions, most likely with heave. For downstream mooring force (in Fig. 9(d)), the key inputs are different. Surge is highly influential, with a moderate S1 and a much larger ST, reflecting its strong role through interactions. Wave frequency also emerges as an important driver: its S1 is small, but ST is significantly larger, suggesting frequency contributes almost entirely via interaction pathways. Wave amplitude and heave remain relevant but less

important than for the upstream case, while solar inputs are negligible.

An important feature of the results is the asymmetry between upstream and downstream mooring forces. The upstream force is primarily governed by heave motion, which directly modulates the vertical displacement and line tension of the mooring lines connected at the wave-facing side. Physically, the upstream line bears the initial impact of wave-induced motions, so its load is most sensitive to the heave amplitude of the platform. By contrast, the downstream force is more sensitive to surge and wave frequency. This reflects the fact that the

Table 3
Performance comparison of the RF model under different data splitting strategies.

Target	R ² for Original Split (80/20)	R ² for New Split (150/5)
Power output/W	0.994	0.994
Temperature of PV panel/°C	0.999	0.999
Mooring force upstream/N	0.986	0.989
Mooring down upstream/N	0.982	0.983
Average	0.990	0.992

downstream line does not experience the direct vertical excitation of waves but is influenced by the longitudinal oscillations of the floating structure, which depend strongly on surge dynamics and frequency-dependent resonance. Surge contributes predominantly through interaction effects, as the downstream line tension builds up when horizontal oscillations combine with periodic forcing from incident waves. This difference in sensitivity patterns underscores the distinct mechanical roles of upstream and downstream moorings: upstream force is wave-impact and heave dominated, while downstream force is governed by horizontal motions and their resonance characteristics.

3.3. Showcases of the real-time digital twin for the floating photovoltaic prototype

To demonstrate the capability of the proposed digital twin framework, real-time showcases were conducted by coupling the laboratory-scale floating photovoltaic (FPV) prototype with its Unity-based virtual replica. Representative cases are illustrated in Fig. 10 and Fig. 11, where the physical tank tests (top panels) are directly compared with the synchronised digital twin visualisations (middle panels). The bottom panels show time series of the principal motion variables—heave, surge, and pitch—together with the predicted performance indicators, including power output, upstream and downstream mooring forces, and PV panel temperature. The demo video, together with supplementary resources, can be found in Appendix 1.

The two figures correspond to different solar incidence angles: Fig. 10 represents normal incidence (90°), whereas Fig. 11 corresponds to a slanted incidence (45°). In both cases, the digital twin was able to reproduce the dynamic response of the FPV system with high fidelity, capturing the oscillatory patterns of platform motions and reflecting consistent variations in mooring forces and thermal–electrical outputs.

These showcases highlight the effectiveness of the digital twin in providing a real-time, immersive view of the FPV system. By bridging physical measurements with a virtual environment, the framework not only facilitates visual inspection of hydrodynamic and electrical behaviour but also establishes a foundation for predictive monitoring and control in future large-scale deployments.

It is observed that while the digital twin successfully synchronises primary motion data, slight visual discrepancies remain regarding the rotational amplitude at the extremities of the pontoon. This is attributed to the misalignment between the virtual geometric centre and the physical centre of gravity, which is shifted due to the mass distribution of the PV panels and catamaran floaters. Furthermore, the current model employs a simplified kinematic mapping that does not fully account for the dynamic shifting of the rotation centre caused by mooring line tension. Future research will focus on integrating a high-fidelity multi-body dynamics solver to achieve more precise spatial synchronisation of the FPV's complex degrees of freedom.

To ensure the reproducibility of the proposed digital twin platform, the experimental methodology is structured into four primary hardware requirements and a modular software workflow. Researchers can replicate the digital twin environment by: (i) utilising a wave tank or wave-making facility; (ii) deploying a floating PV unit with a mooring system; (iii) integrating a solar simulator; and (iv) equipping the rig with

the sensor suite specified in the methodology section. The resulting empirical data serves as the training set for the Random Forest algorithm. The digital twin platform is designed for portability; by adapting the provided open-source code to accommodate local sensor parameters and data acquisition protocols, a synchronised digital twin model can be successfully implemented. Detailed technical specifications and on-site demonstrations are available upon request from the corresponding author.

4. Limitations of the laboratory-scale digital twin

While this study demonstrates the technical feasibility of an FPV digital twin, several inherent limitations associated with the laboratory environment must be acknowledged. These constraints define the boundary between a proof-of-concept and a utility-scale offshore application.

First, the mechanical loads on the mooring system in this study are significantly lower than those encountered in real-world scenarios. The maximum tension recorded in our experiments was approximately 15 N, which is far below the ultimate limit state, considering the breaking strength of the mooring lines (454.5 N). Consequently, the current data-driven model cannot accurately quantify prediction errors at extremes, as the training distribution does not include structural failure or snap loads. In actual offshore FPV deployments, mooring forces can escalate to hundreds or even thousands of kilonewtons depending on the array's scale and sea severity, and snapping is highly likely to occur.

Second, a substantial gap exists between laboratory-generated waves and stochastic ocean environments. Our experimental wave amplitudes (0.025–0.0375 m) and wavelengths (1.5–5.0 m) represent a highly controlled, small-scale setup. In contrast, operational offshore sites typically face significant wave heights of 0.5–2.5 m, with wavelengths ranging from 20 m (wind waves) to as much as 800 m (swells). Beyond absolute values, the geometric ratio between the floating module size and the wavelength is a key determinant of the system's hydrodynamic response. In this study, the module-to-wavelength ratio reflects conditions where modules are small relative to the wave, typical of short-period sea states. We recognize that at a full offshore scale, the increased flexibility of the integrated array and the impact of long-period swells would significantly alter the structural loading and energy dissipation patterns.

Third, the impact of wave-induced motion on power generation performance warrants further investigation at larger scales. In this study, sensitivity analysis (Fig. 9(a)) indicates that motion-related variables are secondary drivers compared to solar irradiance and incident angles. This is attributed to the relatively small oscillation amplitudes ($\pm 4^\circ$) and high wave frequencies (0.54–1.02 Hz) in our laboratory setup, which result in limited fluctuations in cumulative power output. However, in real-world offshore conditions, significant wave heights can induce much larger angular displacements and shading effects. Such intense motion would likely elevate the importance of hydrodynamic variables in the predictive model. Future research using full-scale field data will be essential to quantify these effects under extreme sea states.

Fourth, the absence of wind in our experimental setup introduces certain limitations in representing the full complexity of offshore environments. In real offshore FPV applications, wind acts as a primary environmental stressor that directly affects the system's steady drift and dynamic response. Without wind loading, the current study likely underestimates the peak tension in the mooring lines and may not fully capture the coupling motion between wind-induced aerodynamic forces and wave-induced hydrodynamic forces. Furthermore, wind significantly influences the thermal regulation of PV panels through convective cooling; hence, its absence means that the power generation model in this study primarily reflects wave-driven effects while omitting wind-related temperature fluctuations.

Fifth, the resilience of the digital twin against sensor failures and communication dropouts is a crucial factor for its practical offshore

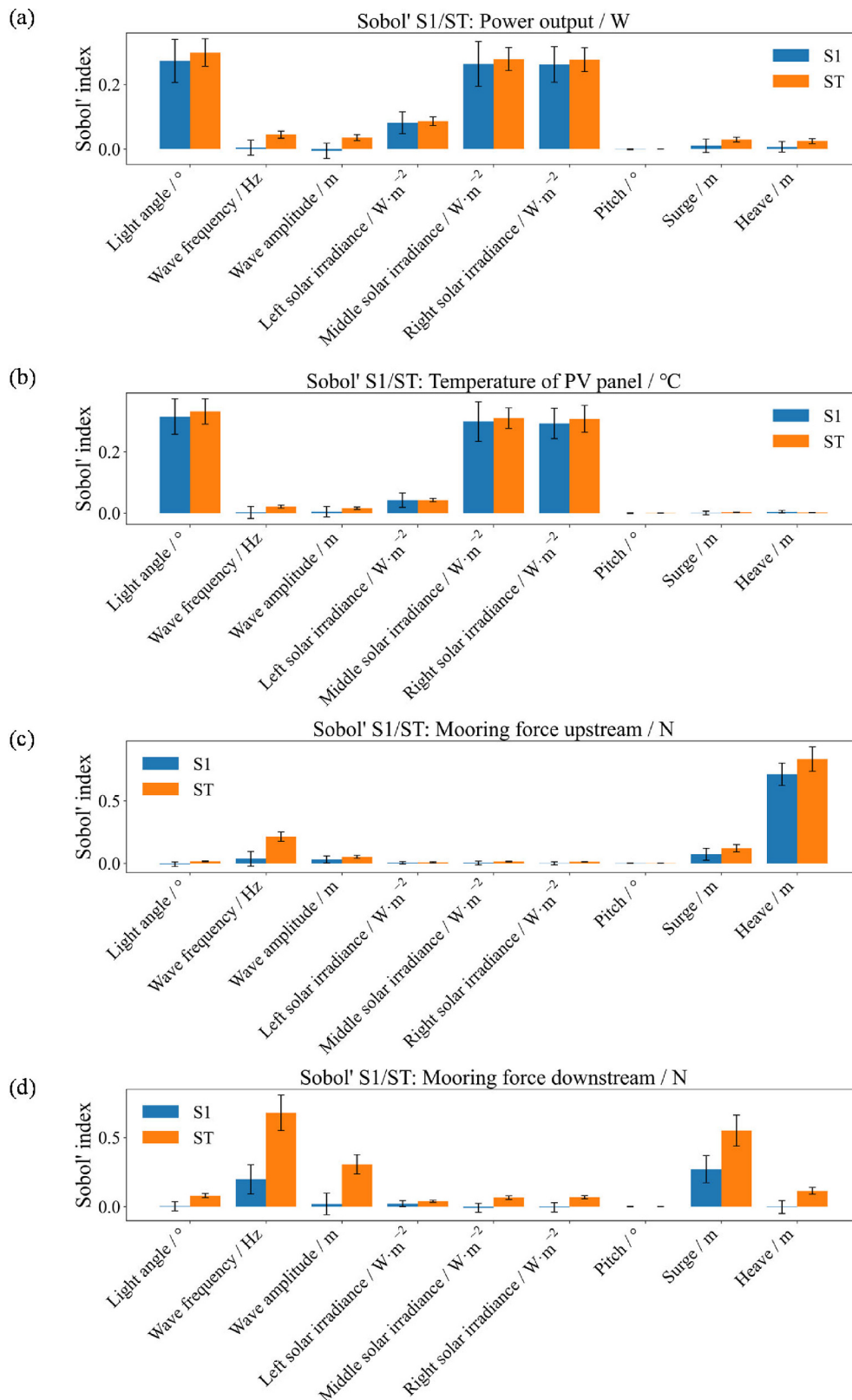


Fig. 9. Sobol' sensitivity indices (S1 and ST) of input features with respect to performance targets: power output, PV panel temperature, and upstream and downstream mooring forces.

deployment. As demonstrated by Hosamo et al. [33], large-scale FPV arrays under irregular waves often face simultaneous data dropouts and optical tracking errors. To mitigate these risks, the digital twin can integrate a two-layer strategy combining advanced preprocessing with

optimized LSTM models to restore missing data with high fidelity. This robust workflow ensures monitoring continuity and preserves reliability-critical statistics, even during sensor malfunctions. Furthermore, beyond the current approach, future research should explore a

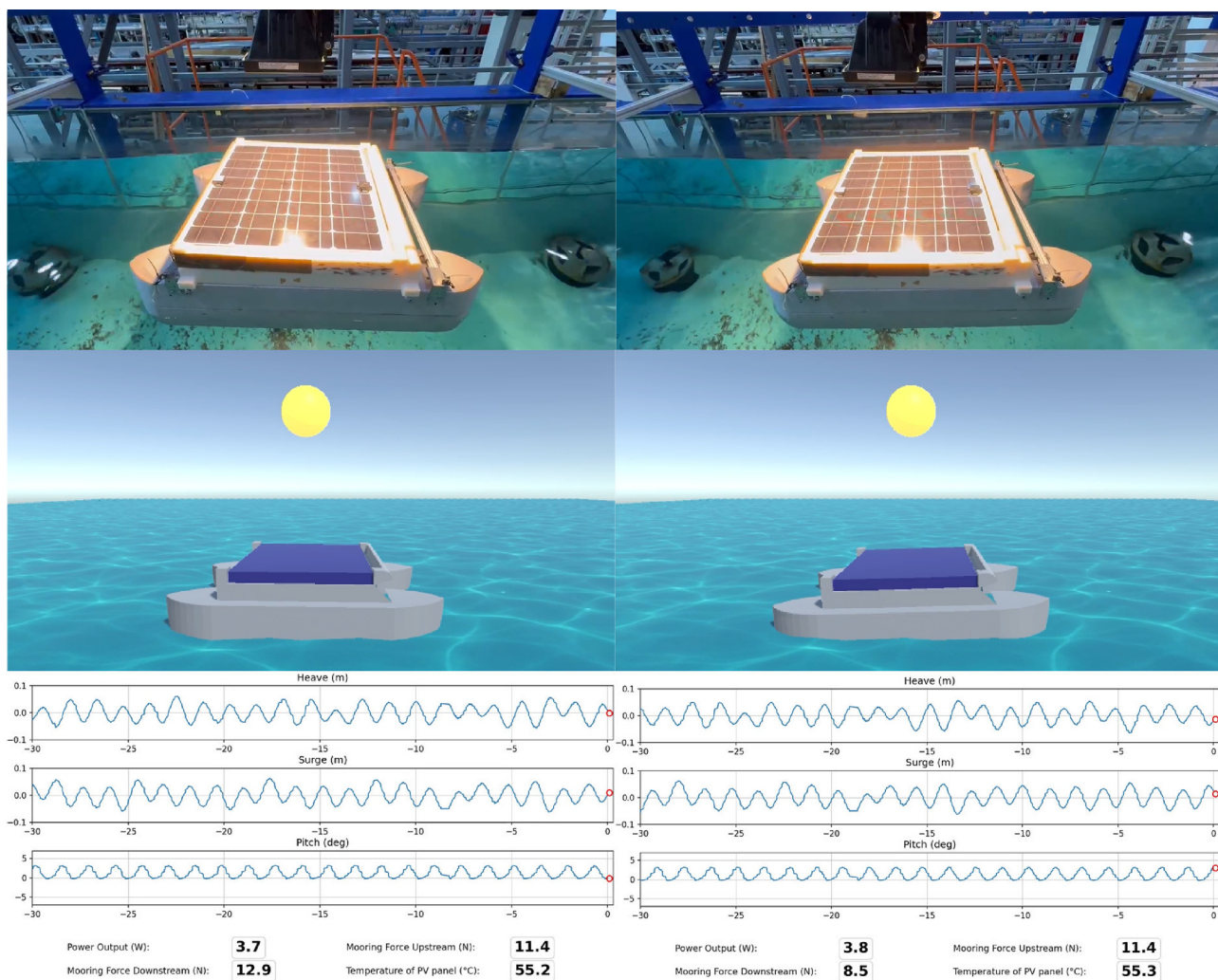


Fig. 10. Showcase of the real-time digital twin of the FPV prototype under normal solar incidence (90°). Top: laboratory experiments in the wave tank; middle: Unity-based digital twin visualisation; bottom: time series of motions (heave, surge, pitch) and performance indicators (power output, mooring forces, panel temperature).

wider range of strategies, such as physics-informed machine learning and multi-sensor fusion, to further enhance the system's fault tolerance in extreme marine environments.

Finally, while this study demonstrates the feasibility of the digital twin framework, we acknowledge that actual offshore power plants typically comprise thousands of interconnected modules. The current model, focused on a single system, does not fully account for the complex multibody interactions and nonlinear connection loads inherent in massive-scale arrays. Future work will focus on extending the modular architecture of the digital twin to accommodate these large-scale interconnected systems, ensuring its applicability to industrial-scale offshore FPV projects.

5. Discussion for the future offshore FPV digital twin

From the current stage of development, the system primarily serves as a laboratory Proof-of-Concept. While the laboratory environment validates the logical closed loop of the digital twin algorithms, the system has not yet reached industrial standards for deployment readiness. Controlled laboratory conditions are far below real offshore environments, which feature random breaking waves, complex wind-wave coupling, and environmental stressors such as high-salinity corrosion and biofouling.

To transition this framework into an industrially capable digital

twin, the model must be retrained using a substantial field dataset. Based on the requirements for cross-environmental generalization, we estimate that the order of magnitude for necessary offshore test cases could reach several thousands. For instance, considering an orthogonal combination of approximately 60 meteorological scenarios (solar radiation cycles under varying wind and rain intensities), 26 wave-height gradients (sampling from 0 to 2.5 m), and 3 critical sensor positions, a dataset exceeding 4680 cases would serve as a baseline to ensure model robustness.

The roadmap for field validation involves deploying a scaled prototype in a real sea area for at least six months to capture seasonal characteristics. Associated costs will focus on procurement of high-protection sensor hardware, wireless transmission for high-frequency sampling data, and regular offshore maintenance. As high-frequency sampling for motion and mooring forces will generate TB-level raw data, the future digital twin must integrate robust reconstruction strategies. Only by utilizing such high-density field data to calibrate laboratory parameters can the system bridge the gap from a laboratory concept to deep-sea deployment readiness.

6. Conclusions

This study has developed and validated a real-time digital twin framework for a FPV prototype by integrating laboratory experiments,

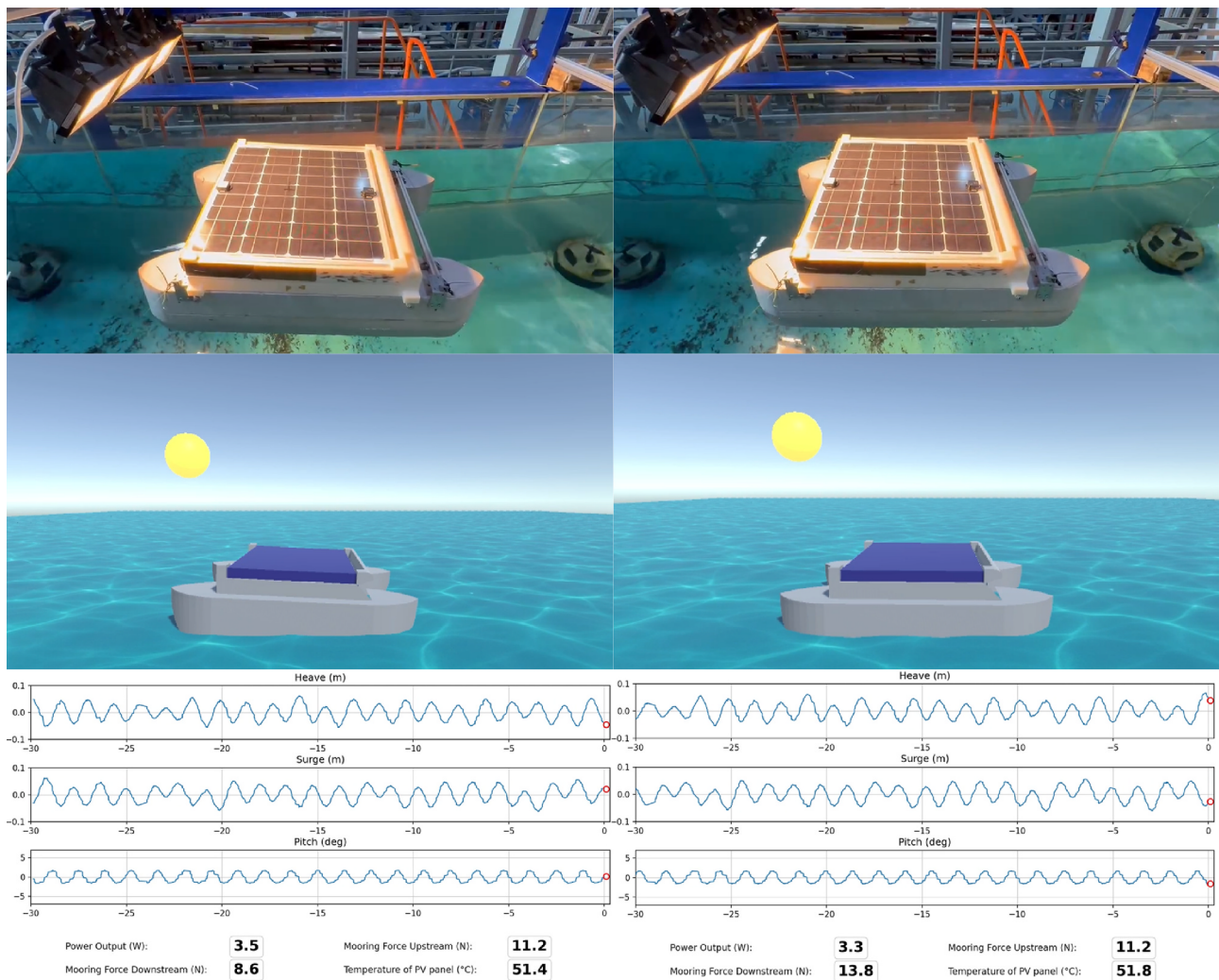


Fig. 11. Showcase of the real-time digital twin of the FPV prototype under slanted solar incidence (45°). Layout as in Fig. 10, demonstrating the close correspondence between physical experiments and the digital twin across dynamic motions and performance outputs.

machine learning, and real-time visualisation. A total of 155 controlled tests were conducted in a wave tank to generate high-resolution datasets, which were used to train a RF model capable of predicting hydro–electro–mechanical responses with high accuracy. The framework demonstrated reliable predictive performance, effective synchronisation between physical and virtual systems, and valuable insights into the governing mechanisms of FPV behaviour, thereby providing a foundation for intelligent monitoring and predictive control in future large-scale deployments. The key findings are as follows:

- 1) The experimental platform combined a solar simulator, FPV prototype, and wave tank, producing datasets across 155 cases under varied irradiance and wave conditions.
- 2) The Random Forest model achieved R^2 values of 0.994 for power output, 0.999 for PV panel temperature, 0.986 for upstream mooring force, and 0.982 for downstream mooring force, with an overall average of 0.990.
- 3) Sensitivity analysis showed that solar inputs (light angle, irradiance) dominated electrical–thermal responses, while hydrodynamic motions (heave, surge) and wave frequency were the main drivers of mooring loads, especially distinguishing upstream from downstream behaviour.
- 4) A real-time Unity-based user interface enabled visualisation and interaction between physical and virtual platforms.

The framework demonstrates scalability, with future research directed towards field-scale validation, hybrid physics–data integration, and advanced machine learning models to capture nonlinear and extreme responses and to support predictive decision-making in offshore FPV applications.

CRediT authorship contribution statement

Danlei Yang: Writing – review & editing, Writing – original draft, Visualization, Validation, Supervision, Software, Methodology, Investigation, Formal analysis, Data curation, Conceptualization. **Chenhao Mi:** Methodology, Investigation. **Xiangcheng Lyu:** Methodology, Investigation. **Ying Xie:** Writing – review & editing, Supervision, Resources. **Zhenhua Luo:** Resources. **Luofeng Huang:** Writing – review & editing, Supervision, Resources, Project administration, Funding acquisition, Conceptualization.

Declaration of competing interest

The authors declare that they have no known competing financial interests or personal relationships that could have appeared to influence the work reported in this paper.

Appendix

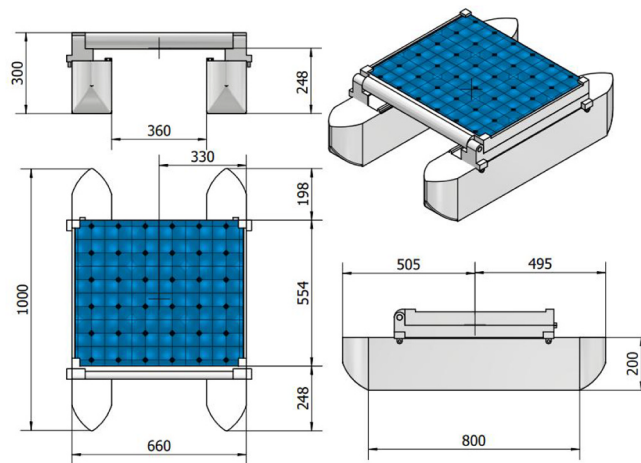
Appendix 1: Resources for the real-time digital twin prototype

All source codes, trained models, demo video, and supporting files used in this study are openly available at the GitHub repository: <https://github.com/DanleiY/Real-time-digital-twin-for-FPV-prototype>.

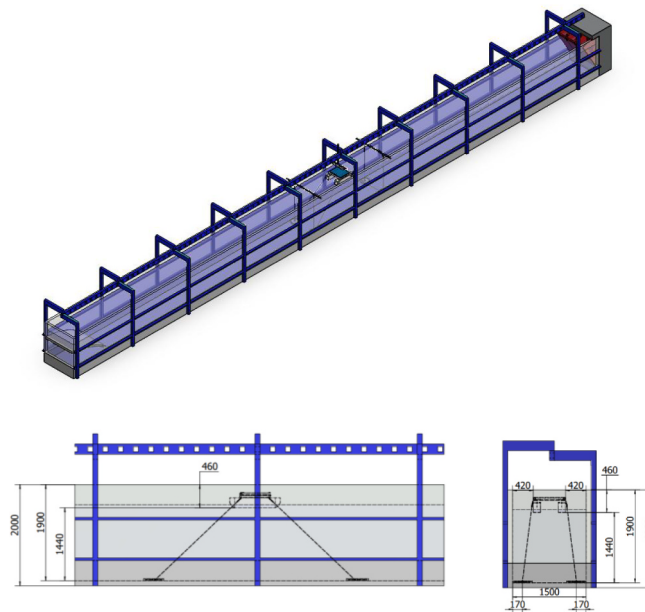
Appendix 2: Experiment setup

Appendix 2 presents the experimental setup employed in this study, which integrates a laboratory-scale floating photovoltaic (FPV) prototype, a mooring system, and a wave tank facility. The FPV structure and its geometric details are illustrated in Appendix Fig. 1, whilst the overall arrangement of the wave tank and mooring layout is shown in Appendix Fig. 2. The full suite of sensors used for data acquisition is summarised in Appendix Table 1, covering force measurement, motion tracking, thermal and electrical monitoring, and irradiance detection. In addition, the parameter configurations for both experimental and control groups are provided in Appendix Table 2, which documents variations in light incidence angle, wave amplitude, and wavelength. Together, these figures and tables offer a comprehensive description of the physical setup and boundary conditions underpinning the digital twin development

For a detailed visual guide of the experimental procedures, please refer to: <https://doi.org/10.5281/zenodo.18714406>.



Appendix Fig. 1. Geometry of the floating PV structure



Appendix Fig. 2. The wave tank facility plus the floating PV system and mooring system

Appendix Table 1

Specifications of all sensors utilized for data acquisition.

Data	Sensor/Equipment	Accordant Software	Data Output Frequency	Additional Notes
Upstream Force	Vernier – Go Direct Force and Acceleration	Vernier Graphical Analysis	10 Hz	RS PRO Steel Extension Spring, 44.6 mm x 9 mm attached
Downstream Force	Vernier – Go Direct Force and Acceleration	Vernier Graphical Analysis	10 Hz	RS PRO Steel Extension Spring, 44.6 mm x 9 mm attached
Motion (Heave, Surge and Pitch)	Witmotion – Accelerometer-Inclinometer	Witmotion	10 Hz	Two placed on PV panel (Upstream and Downstream on PV surface)
Temperature (Ambient, Water and PV Centre)	Thermocouple	Picolog	10 Hz	Thermocouple on the PV surface positioned using heat-resistant tape
Ultrasonic Distance	PEPPERL FUCHS – 60947-5-2	LabView	10 Hz	Two sensors: Upstream and Downstream
Power Output	EL 9000 B Electronic DC Load	EA Power Control	10 Hz	Triangle Configuration: U(A) = 22.83 V, t1 = 0.05 ms, t2 = 0.05 ms. U (Start/End) = 22.83 V, I(Limit) = 2.94A, P(Limit) = 50 W
Irradiance	RS PRO Solar Power Meter ISM410	N/A	One-off reading	Readings taken at upstream, centre and downstream of PV surface to calculate average

Appendix Table 2

Experimental and control case settings with parameter configurations.

Parameters	Number	1	2	3	4	5	6	7	8	9	10	11	12	13	14	15
Experimental group:																
Lights angles/°	5	90	75	60	45	30										
Amplitude/m	2	0.025	0.0375													
Wave length/m	15	1.5	1.75	2	2.25	2.5	2.75	3	3.25	3.5	3.75	4	4.25	4.5	4.75	5
Control group:																
Lights angles/°	5	90	75	60	45	30										
Amplitude/m	0	0														
Wave length/m	0	0														
Sum of cases	155															

Data availability

Data will be made available on request.

References

- Gadzanku S, Mirlatz H, Lee N, Daw J, Warren A. Benefits and critical knowledge gaps in determining the role of floating photovoltaics in the energy-water-food nexus. *Sustainability (Switzerland)* 2021;13. <https://doi.org/10.3390/su13084317>.
- Cazzaniga R, Rosa-Clot M. The booming of floating PV. *Sol Energy* 2021;219:3–10. <https://doi.org/10.1016/j.solener.2020.09.057>.
- Kjeldstad T, Lindholm D, Marstein E, Selj J. Cooling of floating photovoltaics and the importance of water temperature. *Sol Energy* 2021;218:544–51. <https://doi.org/10.1016/j.solener.2021.03.022>.
- El Hammoumi A, Chitita S, Motahhir S, El Ghzizal A. Solar PV energy: from material to use, and the most commonly used techniques to maximize the power output of PV systems: a focus on solar trackers and floating solar panels. *Energy Rep* 2022;8: 11992–2010. <https://doi.org/10.1016/j.egy.2022.09.054>.
- Stiubiner U, de Freitas AG, Heilala J, Fuser I. PV to reduce evaporative losses in the channels of the São Francisco's River water transposition project. *Sci Rep* 2024; 14. <https://doi.org/10.1038/s41598-024-56952-z>.
- Wood Mackenzie. *Floating solar landscape 2024*; 2024.
- Silalahi DF, Blakers A. Global Atlas of Marine floating Solar PV potential. *Solar* 2023;3:416–33. <https://doi.org/10.3390/solar3030023>.
- Delacroix S, Bourdier S, Soulard T, Elzaabalawy H, Vasilenko P. Experimental modelling of a floating solar power plant array under wave forcing. *Energies (Basel)* 2023;16. <https://doi.org/10.3390/en16135198>.
- Huang L, Yang Y, Khojasteh D, Ou B, Luo Z. Floating solar power loss due to motions induced by ocean waves: an experimental study. *Ocean Eng* 2024;312. <https://doi.org/10.1016/j.oceaneng.2024.118988>.
- Kaymak MK, Şahin AD. Problems encountered with floating photovoltaic systems under real conditions: a new FPV concept and novel solutions. *Sustainable Energy Technol Assess* 2021;47. <https://doi.org/10.1016/j.seta.2021.101504>.
- Choi YK, Lee JH. Structural safety assessment of ocean-floating photovoltaic structure model. *Isr J Chem* 2015;55:1081–90. <https://doi.org/10.1002/ijch.201400197>.
- Lee JH, Paik KJ, Lee SH, Hwangbo J, Ha TH. Experimental and numerical study on the characteristics of motion and load for a floating solar power farm under regular waves. *J Mar Sci Eng* 2022;10. <https://doi.org/10.3390/jmse10050565>.
- Hu C, Sueyoshi M, Liu C, Kyojzuka Y, Ohya Y. Numerical and experimental study on a floating platform for offshore renewable energy; 2013.
- Jiang Z, Dai J, Saettone S, Tørå G, He Z, Bashir M, et al. Design and model test of a soft-connected lattice-structured floating solar photovoltaic concept for harsh offshore conditions. *Mar Struct* 2023;90. <https://doi.org/10.1016/j.marstruc.2023.103426>.
- Friel D, Karimirad M, Whittaker T, Doran J. Experimental hydrodynamic assessment of a cylindrical-type floating solar system exposed to waves. *J Ocean Eng Sci* 2023;8:461–73. <https://doi.org/10.1016/j.joes.2023.08.004>.
- Qu X, Yao Y, Du J. Conceptual design and hydrodynamic performance of a modular hybrid floating foundation. *Energies (Basel)* 2021;14. <https://doi.org/10.3390/en14227605>.
- Bi C, Law AWK. Co-locating offshore wind and floating solar farms – effect of high wind and wave conditions on solar power performance. *Energy* 2023;266. <https://doi.org/10.1016/j.energy.2022.126437>.
- Zhang C, Wang P, Huang L, Zhang M, Wu H, Ning D. Resonance mechanism of hydroelastic response of multi-patch floating photovoltaic structure in water waves over stepped seabed. *Phys Fluids* 2023;35. <https://doi.org/10.1063/5.0169061>.
- Yang Y, Ren K, Zhou B, Sun SY, Huang L. Wave interaction with multiple adjacent floating solar panels with arbitrary constraints. *Phys Fluids* 2024;36. <https://doi.org/10.1063/5.0198106>.
- Benjamins S, Williamson B, Billing SL, Yuan Z, Collu M, Fox C, et al. Potential environmental impacts of floating solar photovoltaic systems. *Renew Sustain Energy Rev* 2024;199. <https://doi.org/10.1016/j.rser.2024.114463>.
- Bossi S, Blasi L, Cupertino G, dell'Erba R, Cipollini A, De Vito S, et al. Floating photovoltaic plant monitoring: a review of requirements and feasible technologies. *Sustainability (Switzerland)* 2024;16. <https://doi.org/10.3390/su16198367>.
- Abiagador HL, Resonable RPL, Calimpusan RACO, Delloso JT, Mendoza R. Design and Development of a Monitoring System for Floating Solar Platforms. 2nd International Conference on Emerging Trends in Information Technology and Engineering, ic-ETITE 2024, Institute of Electrical and Electronics Engineers Inc.; 2024. <https://doi.org/10.1109/ic-ETITE58242.2024.10493552>.
- Make more digital twins n.d.
- Jiang Y, Yin S, Li K, Luo H, Kaynak O. Industrial applications of digital twins. *Philosophical transactions of the Royal Society A: Mathematical Phys Eng Sci* 2021; 379. <https://doi.org/10.1098/rsta.2020.0360>.
- Olayiwola O, Cali U, Elsdon M, Yadav P. Enhanced solar photovoltaic system management and integration: the digital twin concept. *Solar* 2025;5. <https://doi.org/10.3390/solar5010007>.
- Nguyen DT, Hansen Solvberg S, Aas-Hansen T. Digital twin-driven optimal design of connector stiffness for floating multi-modular structures-an application for floating solar energy harvest; 2024.

- [27] Prinsloo FC, Schmitz P, Lombard A. System dynamics characterisation and synthesis of floating photovoltaics in terms of energy, environmental and economic parameters with WELF nexus sustainability features. *Sustainable Energy Technol Assess* 2023;55. <https://doi.org/10.1016/j.seta.2022.102901>.
- [28] Entezari A, Aslani A, Zahedi R, Noorollahi Y. Artificial intelligence and machine learning in energy systems: a bibliographic perspective. *Energ Strat Rev* 2023;45. <https://doi.org/10.1016/j.esr.2022.101017>.
- [29] Khortsriwong N, Boonraksa P, Boonraksa T, Fangsuwannarak T, Boonsrirat A, Pinthurat W, et al. Performance of deep learning techniques for forecasting PV Power generation: a case study on a 1.5 MWp floating PV Power Plant. *Energies (Basel)* 2023;16. <https://doi.org/10.3390/en16052119>.
- [30] Sulaiman MH, Jadin MS, Mustaffa Z, Mohd Azlan MN, Daniyal H. Short-Term forecasting of floating photovoltaic power generation using machine learning models. *Cleaner Energy Syst* 2024;9. <https://doi.org/10.1016/j.cles.2024.100137>.
- [31] Khalifeh Soltani SR, Mostafaeipour A, Mishra P, Alidoost S, Jahangiri M, Abrisham KM. Green hydrogen production and prediction using floating photovoltaic panels on wastewater ponds. *Renew Energy* 2025;243. <https://doi.org/10.1016/j.renene.2025.122554>.
- [32] RandomForestRegressor. <https://scikit-learn.org/stable/modules/generated/sklearn.ensemble.RandomForestRegressor.html> n.d.
- [33] Hosamo H, Hosamo M, Dai J, Jiang Z. Efficient monitoring and prediction of the motion responses of compliant floating photovoltaic arrays: Case study of a hydrodynamic model test with erroneous sensor data. *Results Eng* 2025;28. <https://doi.org/10.1016/j.rineng.2025.107625>.

Real-time machine learning-driven digital twin framework of a floating solar system in waves

Yang, Danlei

2026-05-15

Attribution 4.0 International

Yang D, Mi C, Lyu X, et al., (2026) Real-time machine learning-driven digital twin framework of a floating solar system in waves. *Energy Conversion and Management*, Volume 356, May 2026, Article number 121373

<https://doi.org/10.1016/j.enconman.2026.121373>

Downloaded from CERES Research Repository, Cranfield University